Ultrafast Dynamics of Photoexcited Hot Carrier Generation and Injection in AgNWs@TiO2@GNS Nanostructures

Yiwen Li,[†,‡] Jiaji Cheng,[§] Junzi Li,[§] Marie-Hélène Delville,[∥] Mona Tréguer-Delapierre,[∥] Tingchao He,*[,§] Rui Chen,*[,‡] and Zikang Tang*[,†]

[†]The Institute of Applied Physics and Materials Engineering, University of Macau, Avenida da Universidade, Taipa, Macau, P. R. China

[‡]Department of Electrical and Electronic Engineering, Southern University of Science and Technology, Shenzhen, Guangdong 518055, P. R. China

[§]College of Physics and Energy, Shenzhen University, Shenzhen, Guangdong 518060, P. R. China

[∥]University of Bordeaux, CNRS, ICMCB, UMR 5026, 87 87 avenue du Dr Albert Schweitzer, 33608 Pessac, France

S *Supporting Information*

ABSTRACT: The generation and injection of hot electrons in plasmonic nanostructures have received a wide-range potential application in the next generation of ultrafast nanophotonics as well as energy harvesting, storage and conversion. In many cases, the energetic carriers with high energy beyond Fermi level are desirable for photochemical reactions due to the tremendous efficient hot electron injection. However, directly electron−electron scattering lifetime observations have few reported and hot electrons generally suffer from a low generation efficiency in conventional plasmonic nanostructures. This paper reports on the fabrication of hybrid AgNWs@TiO2@Au core−shell nanostructures and the investigation of the ultrafast dynamics of their energetic carriers based on interband and intraband excitations through transient absorption spectroscopy measurements. Finally, the different electronic transition processes are discussed in terms of ultrafast decay response, which is necessary to design proper nanostructures aimed at efficient hot electron injection.
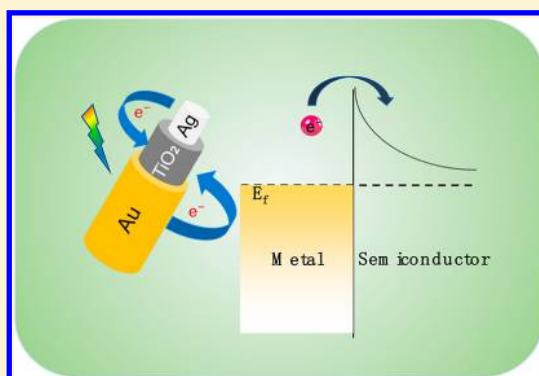
1. INTRODUCTION

Surface plasmon, which derives from the collective oscillation of free conducted electrons in metallic nanoparticles (NPs), contributes to many tremendous advances in nanoscience.[1] These nanoparticles were used in many different areas including optoelectronics and sensors, which are inspired by their superior optical behavior.[2−5] After incident light excitation with resonant energy, electrons undergo a decay through either a radiative channel via scattering, or a nonradiative pathway via electron−hole interaction.[6,7] In particular, the generation and injection of hot electrons in electron−hole pairs are significant for photochemical applications which involve catalysis and photodetectors.[8−11] The hot electron emission also could be enhanced with complicated plasmonic nanostructures.[12] Generally speaking, nonthermal electrons from plasmonic decay after incident light excitation could undergo a non-Fermi distributed before relaxation to Fermi distribution resulted from electron−electron scattering[13] The time scale is around several hundred femtoseconds. The next steps then imply a further cooling process to break the hot thermalized distribution. The corresponding relaxation is induced by an electron−phonon coupling with a time scale of a few picoseconds.[14] Ultrafast dynamics study through

ultrafast transient spectroscopy is then essential to examine plasmonic induced hot electron injection or energy transfer between plasmon and semiconductor.[15−17] Besides, the plasmon-exciton interactions of metal and semiconductor composites have also been investigated via ultrafast techniques for surface catalytic reactions.[18−20]

In the past decades, ordinary nanostructures such as plasmonic metal@metal oxide core−shell nanostructures have been studied through time-resolved optical measurements to discuss the charge or energy transfer dynamics.[17,21,22] Besides, researchers have observed the anomalous pulsewidth-limited relaxation induced by efficient scattering among energetic hot electrons in complicated plasmonic nanostructures.[23,24] Efficient hot electron generation and energy flow are strongly determined by the excitation energy and configuration of the nanostructures such as the nature of the metal and the dielectric layer thickness. However, most of these nanostructures were fabricated with top-down methods such as electron-beam lithography, during which high cost laborious manipu-

ACS Publications
14857
DOI: 10.1021/acs.jpcc.8b05017
J. Phys. Chem. C 2018, 122, 14857−14864

lation is unavoidable. Colloidal wet chemistry can provide a facile approach to a wide variety of NPs synthesis in terms of compositions, sizes, shapes, core−shell structures, and complexity.[25,26] Versatile and scalable hybrid plasmonic nanostructures can then be obtained without relying on high cost instruments like other nanofabrication methods. Moreover, the synthetic process has no limitation for arbitrary materials besides metallic nanoparticles.[27]

Here, desirable plasmonic semiconductor hybrid nanostructures based on silver nanowires (AgNWs) coated with a well-controlled thickness TiO_2 shell were prepared using an overall wet chemistry approach. For subsequent investigation, gold nanoparticles (GNPs) were further grown onto TiO_2 to form a gold nanoshell (GNS) with different thicknesses. Hot carrier dynamics from photoexcited and plasmonic electrons induced through interband and intraband transitions were investigated, and a pulsewidth-limited relaxation induced by electron−electron scattering was observed. Our study shows how the interband and intraband excitations could affect the electron transition process in plasmonic nanostructures. These results provide physical insights into hot electron conditions in multicomponent systems. The observed photophysical process is closely related to hot electron injection, and it is therefore essential in order to understand more in detail the excited state carrier dynamics of nanostructures and to develop the most adapted ones for hot electron devices.[28,29]

2. EXPERIMENTAL SECTION

Materials. Anhydrous ethylene glycol (99.8%), platinum chloride ($PtCl_2$, 99.99+%), silver nitrate ($AgNO_3$, 99%), poly(vinylpyrrolidone) (PVP, MW ∼ 55 000), absolute ethanol (99.9%, Scharlau), titanium(IV) tetraisopropoxide (TTIP, 97%, Aldrich), acetyl acetone (Acac, 99%, Aldrich), (3-aminopropyl)triethoxysilane (APTES, 99%, Aldrich), gold-(III) tetrachloric acid trihydrate ($HAuCl_4·3H_2O$, 99%, Aldrich) and 11-mercaptoundecanoic acid (MUA, 98%, Aldrich) were used without further purification. Ultrapure water (18.2 MOhm cm at 25 °C) was obtained with a Direct-Q3 system (Millipore).

Controlled Deposition of TiO_2 on AgNWs. The deposition of TiO_2 on the AgNWs surface was performed using acetyl acetone as a retardant reagent to control the hydrolysis and polycondensation of the titanium precursor. In an optimized synthesis, an in total 23 mL solution including 20 mL of the as-synthesized MUA functionalized AgNWs (0.08 mg/mL) in pure ethanol and a mixture of 0.25 mL of Milli-Q water and 2.75 mL of absolute ethanol were introduced in a 50 mL flat-bottom flask with stirring as a template solution. In parallel, 1 mL of the precursor solution at a concentration of 14 mM TTIP mixed with Acac (1:2 molar ratio) was prepared. The precursor solution was then diluted with various fractions of pure ethanol. The thickness of the TiO_2 coating was effectively dependent on the degree of dilution, typically to obtain 5, 10, 20, 50, and 70 nm thickness of TiO_2, the precursor solution must be diluted 10, 5, 4, 3, and 2 times respectively via addition of pure ethanol. 1 mL of either of these light yellow solutions was then injected into the template solution at a rate of 1 mL/h with a syringe pump. After the completion of the injection, the resulting colloidal suspension was heated at 80 °C under stirring for 1.5 h for the condensation procedure to be completed. The colloidal suspension was then washed by 5 extensive centrifugation cycles with pure EtOH and eventually stored in 25 mL pure

ethanol at a concentration of approximately 0.5, 0.8, 1.4, 1.9, and 2.1 mg/mL for ca. 5, 10, 20, 50, and 70 nm TiO_2 thickness samples, respectively. The obtained colloidal suspensions hereafter named as AgNWs@TiO_2 are then ready for the next step. In any case, for large production, the reaction can simply be scaled up to 10−20 times.

Synthesis of AgNWs@TiO_2@APTES-GNPs. Typically, 0.1 mL, $10.88 × 10^3$ nM of as-synthesized APTES-GNPs was diluted ten times with 0.9 mL of pure water and sonicated for 10 min before use. Then 1 mL of 0.1 mg/mL AgNWs@TiO_2 was added to the APTES-GNPs solution with 15 min sonication. The mixture was kept overnight at room temperature in a roller-mixer at a rate of 250 rpm/min. Then, the mixture was washed 3 times with pure water, precipitated by centrifugation and eventually kept in 2 mL pure water at a concentration of ∼0.06 mg/mL. The obtained colloidal suspension, hereafter named as AgNWs@TiO_2@APTES-GNPs, is then ready for the next step. For large production, the reaction can be simply scaled up to 10−20 times.

Step by Step Regrowth of APTES-GNPs for Uniform GNS Formation. After obtaining AgNWs@TiO_2@APTES-GNPs, a layer of GNS could then be achieved by a seed-mediated step by step growth of APTES-GNPs. To do this, a gold precursor solution was prepared, in which 8 mL, 25 mM of $HAuCl_4$ was added to 92 mL of pure water with 300 mg of K_2CO_3. The solution was stirred for 30 min to obtain a colorless solution and kept at 4 °C for 2 days before any use. Then in a typical run of regrowth of GNS, 1 mL of this gold precursor was added to 23 mL of a solution consisting of 4 mL of 0.06 mg/mL AgNWs@TiO_2@APTES-GNPs, 19 mL of pure water and 10 mL of 10 g/L PVP (∼29 000 MW). After 1 min vortex in a falcon, 50 μL of formaldehyde was added to the solution, which was then kept in roller-mixer overnight at a rate of 250 rpm/min. Afterward, the solution was washed 4 times with pure water, precipitated by centrifugation and eventually kept in 4 mL pure water for TEM observation and UV−vis characterizations. To further grow the GNS, such an experiment can be run repeatedly until the desired layer is achieved and typically, with 4 times regrowth, a thin layer of gold can be obtained.

One-Pot Regrowth of APTES-GNPs for Uniform GNS Formation. As indicated from previous experimental details, for 4 mL of 0.06 mg/mL AgNWs@TiO_2@APTES-GNPs, 4 mL of gold precursor is needed for a thin layer formation. In this way, for a one-pot regrowth of APTES-GNPs, a 4 mL gold precursor solution (2 mM) was directly added to 4 mL of 0.06 mg/mL AgNWs@TiO_2@APTES-GNPs with 16 mL of pure water and 10 mL of 10 g/L PVP (∼29 000 MW) while other experimental conditions were kept unchanged. Then, the shell thickness could be controlled by tuning the amount of gold precursor. With 4, 8, and 12 mL of gold precursor (2 mM), the corresponding thicknesses of GNS were around 30, 45, 60 nm, respectively.

Characterization. Transmission electron microscope (TEM) characterizations were performed with a JEOL JEM-1400 Plus microscope operating at 120 kV. The samples were prepared as follows: colloids were diluted in ethanol, and one drop of the diluted suspension was deposited on a copper grid coated with a carbon membrane. Chemical analysis was carried out by STEM coupled to EDX were acquired with a JEOL 2200 FS equipped with a field emissive gun, operating at 200 kV and with a point resolution of 0.23 nm. The UV−vis measurement was performed with a TU-1901 double-beam
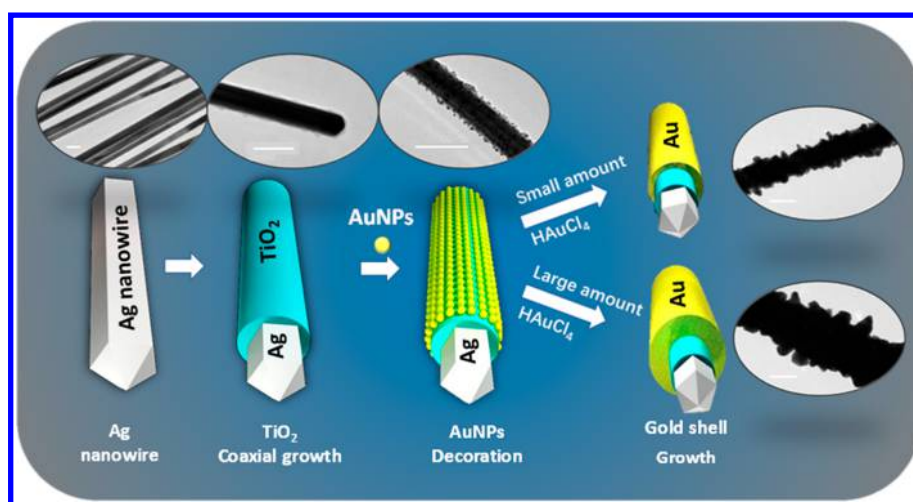
Figure 1. Schematic representative synthesis of the AgNWs@TiO$_2$@GNS heterostructures with thin and thick GNS. White pentagonal prism stands for Ag, cyan coating stands for the TiO$_2$ layer, and the light-yellow particles and walls are GNPs and GNS. The corresponding TEM images are around the schemes. All scale bars: 100 nm.
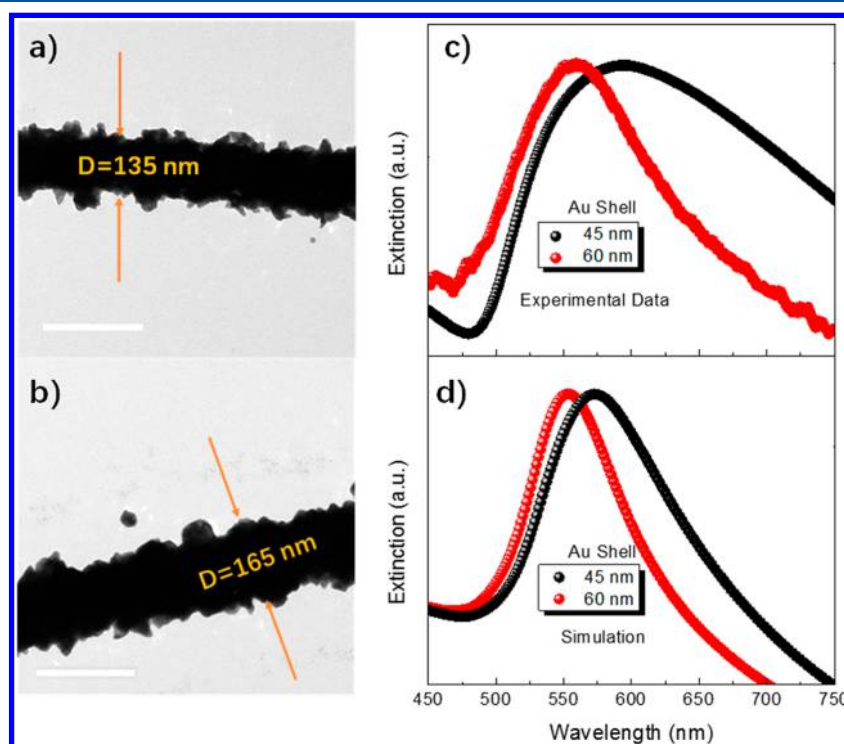

Figure 2. (a, b) Representative TEM images of the nanoheterostructures and (c) experimental and (d) calculated extinction spectra of AgNWs/TiO$_2$/GNS with 45 and 60 nm thicknesses of GNS. All scale bars: 200 nm.

UV/vis spectrophotometer (Beijing Purkine General Instrument Co. Ltd., China)

Optical Simulation. The simulated extinction spectra and field enhancement were performed using a three-dimensional module on Finite-difference time-domain (FDTD) based software (Lumerical Solutions). The model systems include a three-dimensional nanoparticle surrounding with water and the dielectric function data for silver and gold taken from Johnson and Christy.

Transient Absorption Measurements. In this measurement spectra-Physics Solstice were utilized as the ultrafast laser beams with a regeneratively amplified Ti:sapphire laser system (Coherent Legend, 800 nm, 100 fs and 1 kHz repetition rate).

Part of the 800 nm output laser was guided into Traveling Wave Optical Parametric Amplifier (TOPAS) to generate pulse for pump with desirable wavelength. The power of the pump pulses could be controlled with a series of neutral-density filter wheels. The pump beam was focused at the sample with a spot diameter about 200 μm as following chopped by as synchronized chopper at 333 Hz. The probe beams in the wavelengths between 350 and 800 nm were achieved by supercontinuum generation from a thin CaF$_2$ plate. The probe pulses were focused into a fiber-coupled multichannel spectrometer with complementary metal-oxide-semiconductor (CMOS) sensors with detecting at a frequency of 1 kHz. The delay between the pump and probe pulses was
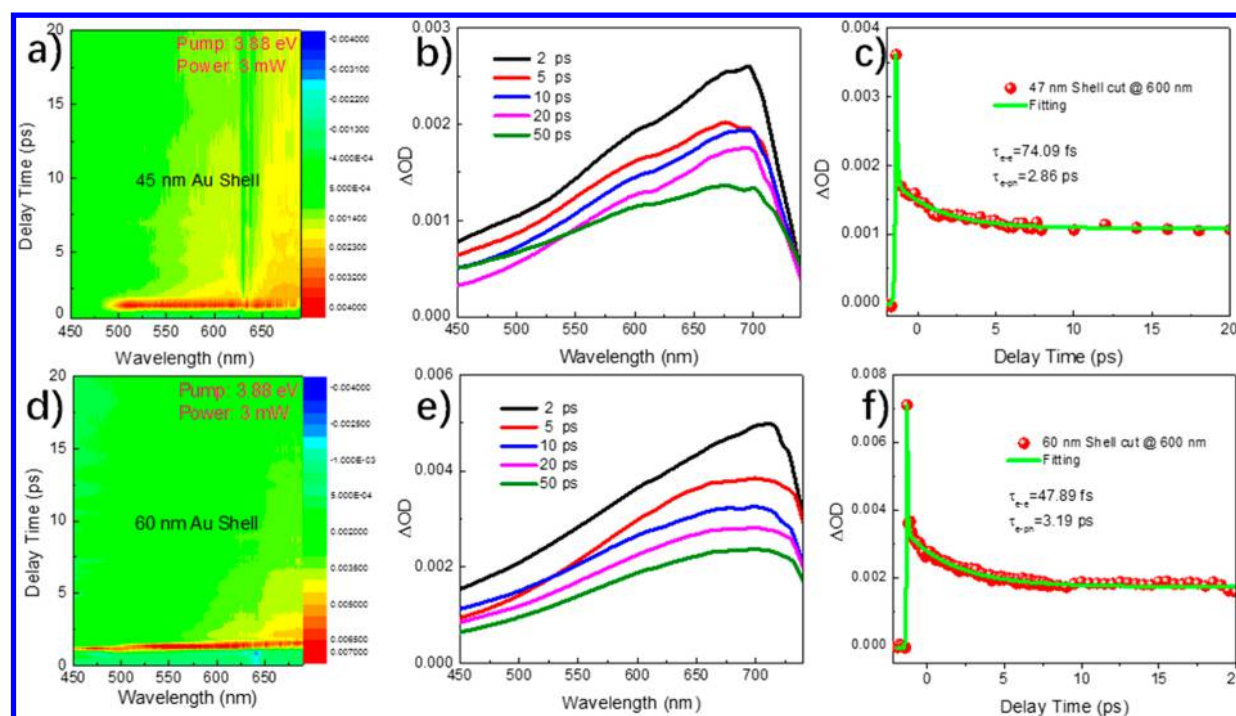
Figure 3. Transient absorption measurements of the AgNW@TiO$_2$@GNS with interband excitation. ΔOD spectral mapping of AgNWs@TiO$_2$ with 45 nm (a) and 60 nm (d) GNS. Transient absorption spectra at various time delays of AgNWs@TiO$_2$ with 45 nm (b) and 60 nm (e) GNS. Time dynamics of cut at 600 nm for AgNWs@TiO$_2$ with 45 nm (c) and 60 nm (f) GNS. All the experiments were performed under pump energy of 3.88 eV with average power of 3 mW.

controlled by a motorized delay stage. The aqueous samples were dispersed without bubble in a 1 mm cuvette, and both beams of pump and probe lasers were spatially overlapped onto the cuvette.

3. RESULTS AND DISCUSSION

Morphology and Steady State Optical Measurements of Hybrid Nanostructures. The 35 nm diameter with 3 μm length AgNWs were employed for the synthesis of AgNWs@TiO$_2$@GNPs, which was performed as illustrated in Figure 1 for a TiO$_2$ shell of 5 nm. After that, GNPs were continuously grown to form GNS leading to AgNWs@TiO$_2$@GNS core−shell−shell hybrid nanostructures. To achieve this, gold precursor in water was added to AgNWs@TiO$_2$@GNPs and then reduced slowly to grow the GNPs in each run as shown in the experimental method. The TEM images shown in Figures S1c-f confirm the step-by-step growth of the GNPs and the formation of GNS after four cycles. The corresponding UV−vis spectra (Figure S1g) witness that the characteristic plasmon peak of GNPs undergoes an obvious red shift from 538 to 592 nm. The thickness of the GNS is measured to be around 30 nm based on more than 100 acquisitions. The distribution of silver, titania, and gold within the nanostructures was further investigated by energy-dispersive X-ray spectroscopy (EDX) coupled with scanning transmission electron microscopy (STEM) to map the Ag and Au elements of a AgNWs@TiO$_2$@GNS nanowire with 30 nm GNS (Figure S2). The respective mappings and profiles through the nanowire are consistent with the expected nanostructure. Furthermore, the thickness of GNS can be controlled via a continuous addition of gold precursor.

The thinnest GNS sample with 30 nm exhibits no apparent plasmon response (Figure S3a), which is attributed to

immature formation stage of Ag−Au hybrid nanostructures.[30] Typical samples with 45 and 60 nm thick GNS are presented in Figure 2a,b. Their extinction spectra are blue-shifted from 574 to 559 nm as the GNS thickness increases (Figure 2c), which is consistent to previous reports on gold nanotube.[30,31] The experimental and simulated steady absorption spectra indicate the presence of Ag−Au alloy[30] due to TiO$_2$ etching during gold shell growth leading to metal direct contact partially. Simulation of the electric field distributions are shown in parts b−d of Figure S3, which display strong field enhancement at interface and surface of shell. In addition, the theoretical extinction spectra were calculated via FDTD to quantify the effects of GNS on the optical response of the hybrid nanowires (Figure 2d). During the simulation, Johnson and Christy's data were used and the silver dielectric function was fixed with a uniform surrounding medium ($n = 1.33$). From the simulations presented in Figure 2d, it can clearly be seen that the position of the extinction peaks is basically in qualitative agreement with the experimental UV/vis spectra. The dipole−dipole coupling effect results in a slightly red-shifted and broader peaks in the experimental observation. These samples with different GNS thicknesses were used to study their ultrafast dynamics performance due to their excellent plasmonic behavior.

Ultrafast Dynamics of Hybrids Nanostructure with Interband Excitation. Visible pump−probe transient absorption measurements were utilized to investigate the carrier relaxation dynamics of plasmonic hybrid structures. Figure 3 shows their optical density change (ΔOD) spectrum and temporal evolution. ΔOD is the difference of the material's absorption in wavelength range with and without the pump pulse excitation. All the hybrid nanostructures were excited in the interband transition region with 3.88 eV photo energy and 3 mW pump power. Figure 3a shows the two-dimensional
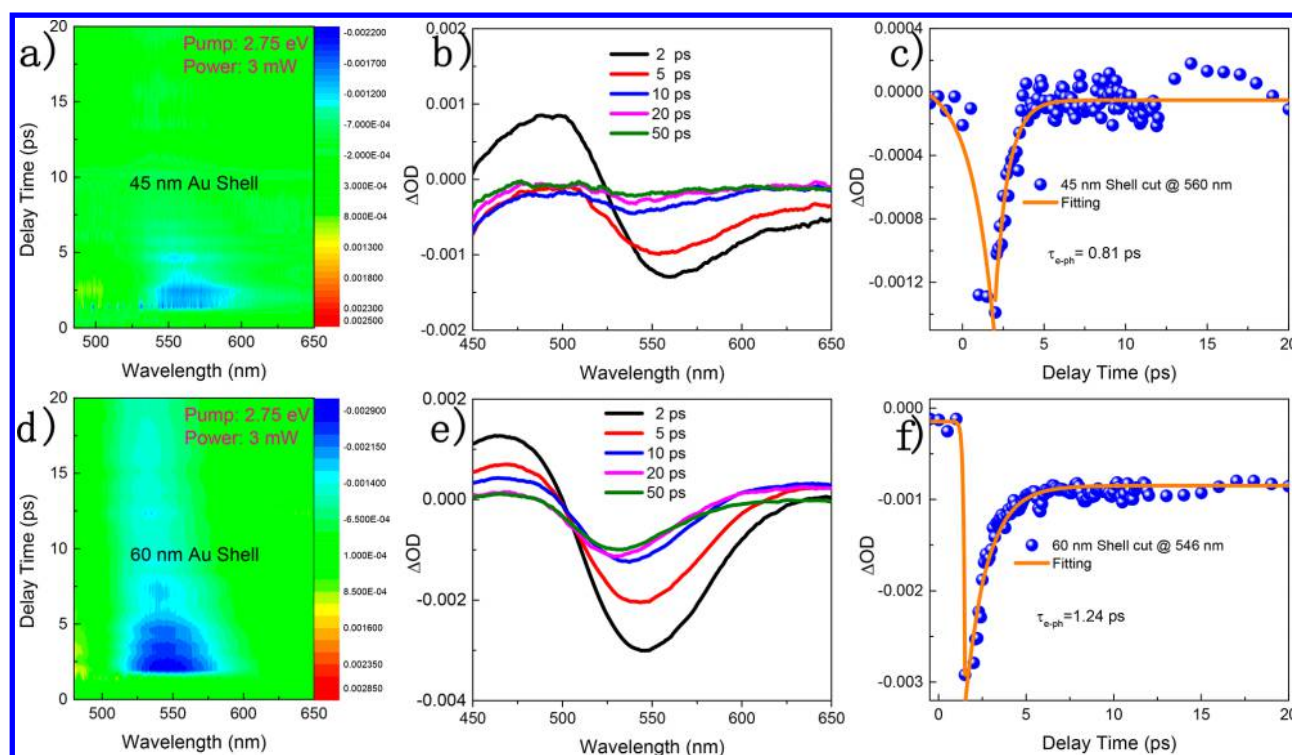
Figure 4. Transient absorption measurements of the AgNW@TiO$_2$@GNS with intraband excitation. ΔOD spectral mapping of AgNWs@TiO$_2$ with 45 (a) and 60 nm (d) GNS. Transient absorption spectra at various time delays of AgNWs@TiO$_2$ with 45 (b) and 60 nm (e) GNS. Time dynamics of cut in photobleaching peaks for AgNWs@TiO$_2$ with 45 (c) and 60 nm (f) GNS. All the experiments were conducted under pump energy of 2.75 eV with an average power of 3 mW.

contour maps (combined with the corresponding spectral and temporal dynamics) of the sample with the 45 nm GNS. In this frequency domain the spectrum does not show any conventional photobleaching signal around the plasmonic peak (located at 574 nm as in the steady-state measurement). Corresponding spectra with various delay times are shown in Figure 3b. In the considered time domain in Figure 3c, the decay can be well-fitted by using two components: a fast femtosecond decay and slow picosecond one. The slow 2.86 ps decay lifetime component which represents the relaxation dynamics of the electron−phonon coupling is consistent with previous reports regarding the electron−phonon coupling for gold nanospheres and nanorods.[14] However, the relaxation also exhibits a much faster decay governed by 74.09 fs with a large pulsewidth-limited ultrafast component (pump laser pulse is 100 fs). In the plasmonic ultrafast dynamics process, the electron−electron scattering happens in this time scale after an extremely short dephasing time below 10 fs.[28] The photoexcited electron−hole pairs first form nonthermal distribution, which cannot be described using Fermi−Dirac statistics.[23] This distribution thermalizes and cools the electrons through electron−electron scattering collisions happen faster than 100 fs, subsequently electron−phonon coupling further cools electrons in the picoseconds time scale. Because of the extremely short time scale for electron−electron scattering, it is challenging to observe their dynamics in transient absorption measurement.[6] Therefore, the Rayleigh scattering spectra are usually employed to estimate their electron surface scattering parameter under line width measurement of single plasmonic nanoparticles.[32,33] Recently, a pulsewidth-limited ultrafast relaxation dynamics was reported in hybrid gold nanodisk, which is consist with our current observation.[23,24] The efficient

electron−electron scattering dominates the high energetic hot electrons relaxation whereas the electron−phonon coupling dominates the relaxation pathway for low-energy electrons near the Fermi sea. The theoretical simulation indicated that the thinner (45 nm) insulator was more efficient than the thicker (60 nm) one to generate more energetic hot electrons beyond Fermi energy.[24] Our ultrathin 5-nm TiO$_2$ layer provides a proper prerequisite for such an efficient energetic hot electron generation. Parts d and e of Figure 3 show the color map and transient spectral measurement for the thicker GNS sample, which exhibits a similar behavior: no photobleaching signal as well as a broad absorption. Figure 3f shows the temporal performance, which can also be described by two components: a fast decay with 47.89 fs and a slow one of 3.19 ps. Compared with the thinner sample (74 fs), the shorter electron−electron scattering time indicates slightly stronger collision effect, corresponding to a higher initial electron temperature after excitation. This leads to slower electron−phonon coupling rate (in the picosecond decay range) according to the two-temperature model.[5] In general, the photoexcited electron−hole pairs can undergo different decay pathways including relaxation through electron−electron scattering or hot electron transfer. In the system discussed herein, the TiO$_2$ dielectric layer could serve as an efficient acceptor, and the hot electron transfer process is desirable to occur. TiO$_2$ layer suffered some extent disintegration due to etching effect of gold shell growth, and the hot electron transfer derive from both Au and Ag. In addition, electron−electron scattering and hot electron transfer are two competing pathways during relaxation. The hybrids with the thinner GNS and weak electron−electron scattering effects could result in an efficient hot electron transfer process. On the other hand, the shorter electron−phonon coupling
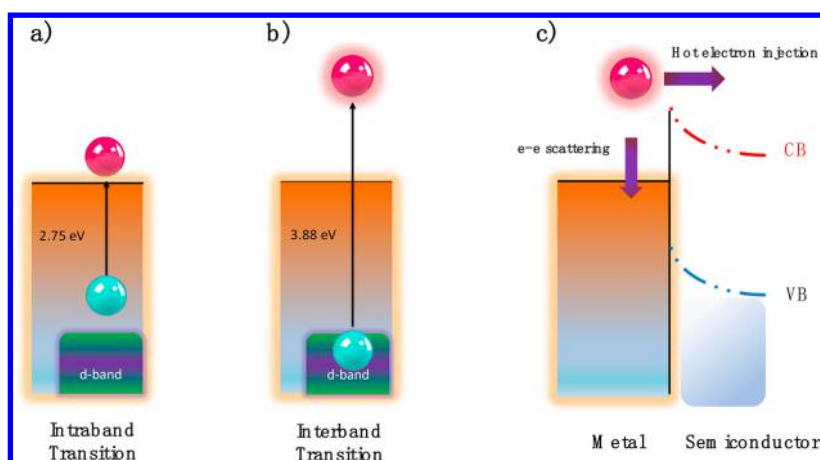
Figure 5. Different electron transition mechanisms described with energy diagrams. (a) Intraband excitation with 2.75 eV to produce electrons near the Fermi surface. (b) Interband excitation with 3.88 eV resulting in energetic electrons. (c) Hot electron transfer process against electron−electron scattering under formation of metal/semiconductor heterojunction.

time also demonstrates the higher efficiency of the hot electron injection.[34,35]

Ultrafast Dynamics of Hybrid Nanostructures with Intraband Excitation. The ultrafast spectroscopy technique was also employed to examine the carrier relaxation for these hybrid plasmonic nanostructures under pumping energy in the intraband excitation. A similar measurement was conducted for both thin and thick GNS samples under 2.75 eV pumping, with power of 3 mW. Conventional photobleaching characteristics located around plasmonic mode at 560 nm for the thinner one (Figure 4a) and 546 nm for the thicker one (Figure 4d) were observed, which was quite different from the interband excitation. It demonstrates that 2.75 eV pump pulses have managed to excite a larger number of electron−hole pairs, which is similar to ground-state bleaching in semiconductors.[14] The increased electron temperature would dramatically change both the real and imaginary part of dielectric function,[36] leading to the slight shift of the bleaching peak (negative signal) and absorption peak wings (positive signal), as shown in Figure 4, parts b and e. Finally, the relaxation dynamics of the excited carriers observed in temporal response shown in Figure 4, parts c and f, give electron−phonon coupling times of 0.81 and 1.24 ps for the thinner and thicker samples, respectively.

The pulsewidth-limited ultrafast relaxation with femto-seconds components is absent in both time-domain measurements. The shorter decay time (0.81 ps) in the thinner GNS nanostructure sample suggests that it is possible to generate a more efficient hot-electron injection. This process would decrease the amount of energy absorbed by the nanostructures, lowering the initial electron temperature in plasmonic materials.

Hot Electron Transition and Relaxation. In frequency domain transient measurements, different optical transient responses are attributed to electron transition mechanisms with different pump wavelengths. It is notable that the d-band energy of Ag−Au alloy was estimated around 3.0 eV for the system based on dielectric function analysis (2.5 eV for Au and 4.0 eV for Ag).[37] The pump energies with 3.88 and 2.75 eV correspond to alloy's interband and intraband transitions, as illustrated in Figure 5. Figure 5a shows an intraband transition between a filled state located 2.75 eV below the Fermi energy (E_f), and an empty state just above E_f. This process is

consistent with a classical surface plasmon excitation, where the subsequent plasmon decays into electron−hole pairs and results in a massive hot electron generation just above the E_f. The plasmonic electrons relaxation back to the filled states below E_f finally leads to the strong photobleaching decay behavior located in their plasmon energy. Our experimental observation shows a silent femtosecond electron−electron scattering component assuming then that the generated carriers are not energetic electrons but instead low energy carriers with energy close to the E_f. However, Figure 5b shows that for an interband transition with extremely high pump energy of 3.88 eV, the excess energy can produce more opportunities to generate the energetic hot electrons well above the E_f. These high energy hot carriers are responsible for the pulsewidth-limited ultrafast femtosecond relaxation component, in contrast with the femtosecond decay absence under intraband excitation. Besides, d-band electrons under interband excitation do not perturb the intraband electrons transition of plasmon excitation.

Their plasmon resonance peak absorption exhibits no reduction after incident pump laser excitation, leading to silent photobleaching signal in transient absorption spectra. The broaden photoinduced absorption signals are also induced by the increase of the imaginary part of the dielectric function under high energy pumping. Figure 5c illustrates a possible hot electron transfer process with a metal contacting a TiO_2 layer. On the basis of previous experimental analyses and simulation, the electron−electron scattering of excited carriers after optical pumping is a competing pathway against the hot electron injection to adjacent semiconductor conduction bands.[34,38] The reason could be the photoexcited hot electrons would lose their energy suffering from a strong electron−electron scattering effect, leading to decrease the population of excited hot carriers with adequate energy to cross the Schottky energy barrier interface. In our case, it is obvious that the thin GNS sample shows the fastest electron−phonon coupling, which indicates an efficient hot electron transfer. In contrast, the thicker one shows a stronger electron−electron scattering process with a faster femtosecond component decay and this is not beneficial for the electron transfer into the TiO_2 semiconductor pathway. Therefore, it is crucial to clarify the different electron transition processes in nanostructures in

order to take advantage of the photoinduced hot electrons or holes for assisted specific photochemical applications.[39,40]

4. CONCLUSION

In summary, hybrid plasmonic nanostructures of AgNWs@ TiO$_2$@GNS with different GNS thicknesses have been synthesized from facile wet chemical approach. Their plasmonic behaviors were studied from steady-state absorption spectra. Optical properties of hot electrons in the plasmonic nanostructures were measured, and their ultrafast dynamics characterized by transient absorption spectroscopy were discussed. The energetic electrons were shown to decay into two ultrafast electron–electron scattering channels on a femtosecond time scale. Our results also show that the selection of the pump light energy is crucial for the generation of efficient energetic hot electrons. The interband and intraband electron transition mechanisms determine the behaviors of the different hot electron dynamics. The insights involved here improved our understanding on efficient hot carrier generation and injection, which is essential for hot electron harvesting in ultrafast nanophotonics and photo-catalysis applications.

ASSOCIATED CONTENT

S **Supporting Information**

The Supporting Information is available free of charge on the ACS Publications website at DOI: 10.1021/acs.jpcc.8b05017.

> TEM and EDX mapping results, theoretical FDTD simulations, and additional figures (PDF)

AUTHOR INFORMATION

Corresponding Authors
*(T.H.) E-mail: tche@szu.edu.cn.
*(R.C.) E-mail: chen.r@sustc.edu.cn.
*(Z.T.) E-mail: zktang@umac.mo.
ORCID ⊙
Jiaji Cheng: 0000-0002-2663-7881
Rui Chen: 0000-0002-0445-7847

Notes
The authors declare no competing financial interest.

ACKNOWLEDGMENTS

REFERENCES

(1) Odom, T. W.; Schatz, G. C. Introduction to Plasmonics. *Chem. Rev.* **2011**, *111*, 3667–3668.
(2) Atwater, H. A.; Polman, A. Plasmonics for Improved Photovoltaic Devices. *Nat. Mater.* **2010**, *9*, 865.
(3) Linic, S.; Christopher, P.; Ingram, D. B. Plasmonic-Metal Nanostructures for Efficient Conversion of Solar to Chemical Energy. *Nat. Mater.* **2011**, *10*, 911.
(4) Li, M.; Cushing, S. K.; Wu, N. Plasmon-Enhanced Optical Sensors: A Review. *Analyst* **2015**, *140*, 386–406.
(5) Mayer, K. M.; Hafner, J. H. Localized Surface Plasmon Resonance Sensors. *Chem. Rev.* **2011**, *111*, 3828–3857.
(6) Hartland, G. V. Optical Studies of Dynamics in Noble Metal Nanostructures. *Chem. Rev.* **2011**, *111*, 3858–3887.
(7) Hartland, G. V.; Besteiro, L. V.; Johns, P.; Govorov, A. O. What's So Hot About Electrons in Metal Nanoparticles? *ACS Energy Lett.* **2017**, *2*, 1641–1653.
(8) Brongersma, M. L.; Halas, N. J.; Nordlander, P. Plasmon-Induced Hot Carrier Science and Technology. *Nat. Nanotechnol.* **2015**, *10*, 25.
(9) Linic, S.; Aslam, U.; Boerigter, C.; Morabito, M. Photochemical Transformations on Plasmonic Metal Nanoparticles. *Nat. Mater.* **2015**, *14*, 567.
(10) Knight, M. W.; Sobhani, H.; Nordlander, P.; Halas, N. J. Photodetection with Active Optical Antennas. *Science* **2011**, *332*, 702–704.
(11) Aslam, U.; Chavez, S.; Linic, S. Controlling Energy Flow in Multimetallic Nanostructures for Plasmonic Catalysis. *Nat. Nanotechnol.* **2017**, *12*, 1000.
(12) Knight, M. W.; Wang, Y.; Urban, A. S.; Sobhani, A.; Zheng, B. Y.; Nordlander, P.; Halas, N. J. Embedding Plasmonic Nanostructure Diodes Enhances Hot Electron Emission. *Nano Lett.* **2013**, *13*, 1687–1692.
(13) Boerigter, C.; Aslam, U.; Linic, S. Mechanism of Charge Transfer from Plasmonic Nanostructures to Chemically Attached Materials. *ACS Nano* **2016**, *10*, 6108–6115.
(14) Jain, P. K.; Qian, W.; El-Sayed, M. A. Ultrafast Electron Relaxation Dynamics in Coupled Metal Nanoparticles in Aggregates. *J. Phys. Chem. B* **2006**, *110*, 136–142.
(15) Cushing, S. K.; Wu, N. Progress and Perspectives of Plasmon-Enhanced Solar Energy Conversion. *J. Phys. Chem. Lett.* **2016**, *7*, 666–675.
(16) Cushing, S. K.; Li, J.; Meng, F.; Senty, T. R.; Suri, S.; Zhi, M.; Li, M.; Bristow, A. D.; Wu, N. Photocatalytic Activity Enhanced by Plasmonic Resonant Energy Transfer from Metal to Semiconductor. *J. Am. Chem. Soc.* **2012**, *134*, 15033–15041.
(17) Li, J.; Cushing, S. K.; Meng, F.; Senty, T. R.; Bristow, A. D.; Wu, N. Plasmon-Induced Resonance Energy Transfer for Solar Energy Conversion. *Nat. Photonics* **2015**, *9*, 601.
(18) Lin, W.; Shi, Y.; Yang, X.; Li, J.; Cao, E.; Xu, X.; Pullerits, T.; Liang, W.; Sun, M. Physical Mechanism on Exciton-Plasmon Coupling Revealed by Femtosecond Pump-Probe Transient Absorption Spectroscopy. *Mater. Today Phys.* **2017**, *3*, 33–40.
(19) Lin, W.; Cao, E.; Zhang, L.; Xu, X.; Song, Y.; Liang, W.; Sun, M. Electrically Enhanced Hot Hole Driven Oxidation Catalysis at the Interface of a Plasmon-Exciton Hybrid. *Nanoscale* **2018**, *10*, 5482–5488.
(20) Cao, E.; Guo, X.; Zhang, L.; Shi, Y.; Lin, W.; Liu, X.; Fang, Y.; Zhou, L.; Sun, Y.; Song, Y.; et al. Electrooptical Synergy on Plasmon–Exciton-Codriven Surface Reduction Reactions. *Adv. Mater. Interfaces* **2017**, *4*, 1700869.
(21) Li, J.; Cushing, S. K.; Bright, J.; Meng, F.; Senty, T. R.; Zheng, P.; Bristow, A. D.; Wu, N. Ag@Cu2o Core-Shell Nanoparticles as Visible-Light Plasmonic Photocatalysts. *ACS Catal.* **2013**, *3*, 47–51.
(22) Cushing, S. K.; Li, J.; Bright, J.; Yost, B. T.; Zheng, P.; Bristow, A. D.; Wu, N. Controlling Plasmon-Induced Resonance Energy Transfer and Hot Electron Injection Processes in Metal@Tio2 Core–Shell Nanoparticles. *J. Phys. Chem. C* **2015**, *119*, 16239–16244.
(23) Sykes, M. E.; Stewart, J. W.; Akselrod, G. M.; Kong, X.-T.; Wang, Z.; Gosztola, D. J.; Martinson, A. B. F.; Rosenmann, D.; Mikkelsen, M. H.; Govorov, A. O.; et al. Enhanced Generation and Anisotropic Coulomb Scattering of Hot Electrons in an Ultra-Broadband Plasmonic Nanopatch Metasurface. *Nat. Commun.* **2017**, *8*, 986.
(24) Harutyunyan, H.; Martinson, A. B. F.; Rosenmann, D.; Khorashad, L. K.; Besteiro, L. V.; Govorov, A. O.; Wiederrecht, G.

P. Anomalous Ultrafast Dynamics of Hot Plasmonic Electrons in Nanostructures with Hot Spots. *Nat. Nanotechnol.* **2015**, *10*, 770.

(25) Rycenga, M.; Cobley, C. M.; Zeng, J.; Li, W.; Moran, C. H.; Zhang, Q.; Qin, D.; Xia, Y. Controlling the Synthesis and Assembly of Silver Nanostructures for Plasmonic Applications. *Chem. Rev.* **2011**, *111*, 3669−3712.

(26) Gargiulo, J.; Cerrota, S.; Cortés, E.; Violi, I. L.; Stefani, F. D. Connecting Metallic Nanoparticles by Optical Printing. *Nano Lett.* **2016**, *16*, 1224−1229.

(27) Zhang, S.; Geryak, R.; Geldmeier, J.; Kim, S.; Tsukruk, V. V. Synthesis, Assembly, and Applications of Hybrid Nanostructures for Biosensing. *Chem. Rev.* **2017**, *117*, 12942−13038.

(28) Besteiro, L. V.; Kong, X.-T.; Wang, Z.; Hartland, G.; Govorov, A. O. Understanding Hot-Electron Generation and Plasmon Relaxation in Metal Nanocrystals: Quantum and Classical Mechanisms. *ACS Photonics* **2017**, *4*, 2759−2781.

(29) Govorov, A. O.; Zhang, H.; Gun'ko, Y. K. Theory of Photoinjection of Hot Plasmonic Carriers from Metal Nanostructures into Semiconductors and Surface Molecules. *J. Phys. Chem. C* **2013**, *117*, 16616−16631.

(30) Sun, Y. Silver Nanowires - Unique Templates for Functional Nanostructures. *Nanoscale* **2010**, *2*, 1626−1642.

(31) Kohl, J.; Fireman, M.; O'Carroll, D. M. Surface Plasmon and Photonic Mode Propagation in Gold Nanotubes with Varying Wall Thickness. *Phys. Rev. B: Condens. Matter Mater. Phys.* **2011**, *84*, 235118.

(32) Sönnichsen, C.; Franzl, T.; Wilk, T.; von Plessen, G.; Feldmann, J.; Wilson, O.; Mulvaney, P. Drastic Reduction of Plasmon Damping in Gold Nanorods. *Phys. Rev. Lett.* **2002**, *88*, 077402.

(33) Hu, M.; Novo, C.; Funston, A.; Wang, H.; Staleva, H.; Zou, S.; Mulvaney, P.; Xia, Y.; Hartland, G. V. Dark-Field Microscopy Studies of Single Metal Nanoparticles: Understanding the Factors That Influence the Linewidth of the Localized Surface Plasmon Resonance. *J. Mater. Chem.* **2008**, *18*, 1949−1960.

(34) Ratchford, D. C.; Dunkelberger, A. D.; Vurgaftman, I.; Owrutsky, J. C.; Pehrsson, P. E. Quantification of Efficient Plasmonic Hot-Electron Injection in Gold Nanoparticle−TiO$_2$ Films. *Nano Lett.* **2017**, *17*, 6047−6055.

(35) Wang, L.; Wang, Z.; Wang, H.-Y.; Grinblat, G.; Huang, Y.-L.; Wang, D.; Ye, X.-H.; Li, X.-B.; Bao, Q.; Wee, A.-S.; et al. Slow Cooling and Efficient Extraction of C-Exciton Hot Carriers in MoS$_2$ Monolayer. *Nat. Commun.* **2017**, *8*, 13906.

(36) Brown, A. M.; Sundararaman, R.; Narang, P.; Schwartzberg, A. M.; Goddard, W. A.; Atwater, H. A. Experimental and Ab Initio Ultrafast Carrier Dynamics in Plasmonic Nanoparticles. *Phys. Rev. Lett.* **2017**, *118*, 087401.

(37) Rioux, D.; Vallières, S.; Besner, S.; Muñoz, P.; Mazur, E.; Meunier, M. An Analytic Model for the Dielectric Function of Au, Ag, and Their Alloys. *Adv. Opt. Mater.* **2014**, *2*, 176−182.

(38) Wu, K.; Rodríguez-Córdoba, W. E.; Yang, Y.; Lian, T. Plasmon-Induced Hot Electron Transfer from the Au Tip to Cds Rod in Cds-Au Nanoheterostructures. *Nano Lett.* **2013**, *13*, 5255−5263.

(39) Zhao, J.; Nguyen, S. C.; Ye, R.; Ye, B.; Weller, H.; Somorjai, G. A.; Alivisatos, A. P.; Toste, F. D. A Comparison of Photocatalytic Activities of Gold Nanoparticles Following Plasmonic and Interband Excitation and a Strategy for Harnessing Interband Hot Carriers for Solution Phase Photocatalysis. *ACS Cent. Sci.* **2017**, *3*, 482−488.

(40) Schlather, A. E.; Manjavacas, A.; Lauchner, A.; Marangoni, V. S.; DeSantis, C. J.; Nordlander, P.; Halas, N. J. Hot Hole Photoelectrochemistry on Au@SiO2@Au Nanoparticles. *J. Phys. Chem. Lett.* **2017**, *8*, 2060−2067.